Frictional power dissipation in a seismic ancient fault

Francesco Lazari[1‡], Angela Castagna[2], Stefan Nielsen[3], Ashley Griffith[4], Giorgio Pennacchioni[1], Rodrigo Gomila[1], Phil Resor[5], Chiara Cornelio[6], Giulio Di Toro[1,6*]

[1] Dipartimento di Geoscienze, Università degli Studi di Padova, Padua, Italy

[2] Former Ph.D. student at School of Geography, Geology and the Environment, Leicester University, United Kingdom.

[3] Department of Earth Sciences, Durham University, Durham, United Kingdom

[4] School of Earth Sciences, The Ohio State University, Columbus (OH), USA

[5] Department of Earth and Environmental Sciences, Wesleyan University, Middletown (CT), USA

[6] Sezione Roma 1, Istituto Nazionale di Geofisica e Vulcanologia, Rome, Italy

[‡] Now at EPFL, Lausanne, Switzerland

[*] Corresponding author

Highlights

- Frictional power $\dot{Q}$ [W/m^2] is shear stress times slip rate during faulting
- $\dot{Q}$ controls fault temperature increase and dynamic weakening during earthquakes
- $\dot{Q}$ cannot be estimated by seismological methods
- We use microstructural observations calibrated by experiments to estimate $\dot{Q}$
- $\dot{Q}$ ranges from 4 to 60 MW/m^2 in an upper crustal fault patch

23

Abstract

25   The frictional power per unit area $\dot{Q}$ (product of frictional traction τ and slip rate

26    $\dot{u}$ in MW m^{-2}) dissipated during earthquakes triggers fault dynamic weakening

27   mechanisms that control rupture nucleation, propagation and arrest. Although of

28   great relevance in earthquake mechanics, $\dot{Q}$ cannot, with rare exceptions, be

29   determined by geophysical methods. Here we exploit theoretical, experimental and

30   geological constraints to estimate $\dot{Q}$ dissipated on a fault patch exhumed from 7-9

31   km depth. According to theoretical models, in polymineralic, silicate rocks the

32   amplitude (< 1 mm) of the grain-scale roughness of the boundary between frictional

33   melt (pseudotachylyte) and host rock decreases with increasing $\dot{Q}$. The dependence

34   of grain-scale roughness with $\dot{Q}$ is due to differential melt front migration in the host

35   rock minerals. This dependence is confirmed by friction experiments reproducing

36   seismic slip where pseudotachylytes were produced by shearing tonalite at $\dot{Q}$

37   ranging from 5 to 25 MW m^{-2}. In natural pseudotachylytes across tonalites, the grain-

38   scale roughness broadly decreases from extensional to compressional fault domains

39   where lower and higher $\dot{Q}$ are expected, respectively. Analysis of the natural dataset

40   calibrated by experiments yields $\dot{Q}$ values in the range of 4-60 MW m^{-2} (16 MW m^{-2}

41   average value). These values, estimated in small fault patches, are at the lower end

42   of broad estimates of $\dot{Q}$ (3-300 MW m^{-2}) obtained from frictional tractions (30-300

43   MPa) and fault slip rates (0.1-1 m/s) assumed as typical of upper crustal

44   earthquakes.

1. Introduction

Frictional power dissipation per unit area ($\dot{Q}(t) = \tau(t)\,\dot{u}\,(t)$ in W m^{-2}, or Nm s^{-1}m^{-2} in units commonly used in geodesy and seismology, with: τ frictional traction or shear stress; $\dot{u}$ on-fault slip rate) is a relevant earthquake source parameter (Sibson, 1980). In fact, $\dot{Q}(t)$ results in temperature increase and grain comminution in µm- to cm-thick slipping zones (Sibson, 2003), that activate dynamic weakening mechanisms promoting propagation of seismic ruptures (Rice, 2006; Di Toro et al., 2011; Tullis et al., 2015; Pozzi et al., 2021). However, $\tau(t)$, or the absolute value of frictional traction during seismic slip is transparent, with notable exceptions, to measurements from the Earth's surface (Guatteri and Spudich 2006; Udias et al., 2014). In fact, only the stress drop, not $\tau(t)$, has direct impact on $\dot{u}(t)$ and therefore influences the seismological signature in the radiated waves (Udias et al., 2014). Instead, the absolute stress levels, and hence $\tau(t)\,\dot{u}\,(t)$, could be estimated by inversion analysis (1) from seismic waves if there is a visible rake rotation during seismic slip (Spudich, 1992) and, (2) as recently proposed, with geodetic techniques, from coseismic slip vectors measured along earthquake surface ruptures (Milliner et al., 2022). However, the two above remain exceptional cases. As a consequence, values of $\dot{Q}(t)$ ranging from 3 to 300 MW m^{-2} have been proposed assuming τ and $\dot{u}$ for ideal earthquakes in the continental crust and ranging from 30 to 300 MPa and 0.1 to 1 m s^{-1}, respectively (Fig. 2 in Sibson, 1980). In this study we aim to obtain more rigorous estimates of $\dot{Q}(t)$, which controls the fault strength evolution during the earthquake in the presence of thermal weakening processes, from microstructural analysis of tectonic pseudotachylytes.

68   Tectonic pseudotachylytes are solidified friction melts produced during seismic

69   faulting (Sibson, 1975). Pseudotachylytes have been used to estimate several

70   earthquake source parameters, including the magnitude of frictional traction, rupture

71   directivity, slip weakening distance, energy budgets, focal mechanisms, stress drops,

72   apparent stress, fracture energy, measures of efficiency and hypocentral depths

73   (Sibson, 1975; Maddock et al., 1987; Di Toro et al., 2005; 2006; Hirose and

74   Shimamoto, 2005; Andersen et al., 2008; Pittarello et al., 2008; Beeler et al., 2016;

75   Petley-Ragan et al., 2019; Ferrand et al., 2021; Johnson et al., 2021;

76   Hosseinzadehsabeti et al., 2021). During earthquakes, seismic rupture propagation

77   (at a few km/s) induces intense and abrupt near-tip stress perturbations that result in

78   host rock fracturing, grain comminution and flash heating (Reches and Dewers,

79   2005; Rice, 2006). In silicate rocks, fault slip may result in temperature increase and

80   frictional melting of the comminuted materials and their host rocks close to the fault

81   surface (Swanson, 1992; Spray, 1995). At this stage and in the few seconds

82   following seismic slip, the melt-rock boundary migrates into the host rocks (Fialko

83   and Khazan, 2006; Nielsen et al., 2008). The melt intrudes fractures in the host rocks

84   (injection veins) or flows along the fault towards dilatational jogs and reservoirs (fault

85   veins) (Sibson, 1975). In the case of granitoid rocks, made of feldspars, quartz and

86   biotite, this ultra-fast melting occurs under non-equilibrium conditions (Shand, 1916).

87   Along the migrating melt-rock boundary, minerals with low melting temperature T_m

88   (biotite, $T_m \sim 650°C$, Navrotsky, 1995) melt faster than high T_m minerals (for andesine

89   feldspar, An45, and quartz, $T_m \sim 1250°C$ and $T_m \sim 1730°C$, respectively, Navrotsky,

90   1995; Spray, 2010). Differential mineral melting results in a grain-scale roughness of

91   the melt-rock boundary (or pseudotachylyte-host rock boundary, from now on PST-

92   HR, once the melt solidifies): embayments and protrusions form in spatial relation

4

93   with HR biotite and quartz/feldspar grains, respectively (Magloughlin and Spray,

94   1992, and references therein) (Fig. 1). The grain-scale roughness is related to (i)

95   mineral physical properties (T_m and thermal shock properties: Papa et al., 2018) and

96   grain size; (ii) melt temperature; and (iii) rate of the temperature increase in the

97   slipping zone, proportional to $\dot{Q}$. Theoretical analysis, tested by experiments on

98   gabbro, indicates that the higher the $\dot{Q}$, the smoother the PST-HR boundary (Nielsen

99   et al., 2010) (Fig. 1). Here we measure the grain-scale roughness of the PST-HR

100   boundary of natural pseudotachylytes within the Adamello granitoids (tonalite) along

101   the Gole Larghe Fault Zone (Italian Southern Alps; Di Toro and Pennacchioni, 2005).

102   After calibration with dedicated experiments, we estimate $\dot{Q}$.

103   **2. Methods**

104   _Experimental pseudotachylytes_ were produced by shearing hollow cylinders (50/30

105   mm external/internal diameter) of non-altered Adamello tonalite with the rotary

106   machine SHIVA installed at the Istituto Nazionale di Geofisica e Vulcanologia in

107   Rome (Di Toro et al., 2010; for sample preparation see Nielsen et al., 2012). Three

108   experiments (S422, S423 and S475) were conducted at room humidity conditions,

109   target equivalent slip rates V_{eq} of 6.5 m s^{-1} and normal stresses of 40, 20, 30 MPa,

110   respectively (Figure 2, Table 1). During the experiments, normal stress, torque

111   (converted into τ), angular rotations and speeds (converted into equivalent slip

112   distances and slip rates, respectively), and sample shortening were measured at

113   acquisition rates of 2.5 kHz (see Niemeijer et al., 2011 for details about the

114   calibration and data acquisition). We also examined a fourth pseudotachylyte

115   produced in previously published experiments performed on the same Adamello

116   tonalite. This pseudotachylyte was obtained by shearing full cylinders, 25 mm in

117   diameter, at equivalent slip rate of 1.3 m s^{-1} and 20 MPa normal stress using a rotary

118   apparatus at Kyoto University (HVR377 in Di Toro et al., 2006). The temperature

119   evolution with slip displacement in the slipping zone was estimated with 2-

120   dimensional numerical modelling (Supplementary Materials SM1, Cornelio et al.,

121   2019).

122   *Natural pseudotachylytes.* 22 samples were collected from eight pseudotachylyte-

123   bearing wavy faults from the dextral strike-slip Gole Larghe Fault Zone (Di Toro and

124   Pennacchioni, 2005) within the Adamello batholith (Callegari and Brack, 2002). The

125   granitoid rock (tonalite) consists of plagioclase (i.e., andesine, An$_{45}$, 48% modal

126   composition), quartz (29%), biotite (17%) and K-feldspar (6%) with an average grain

127   size of 2 mm (Di Toro and Pennacchioni, 2004; 2005). The fault zone was exhumed

128   from 7-9 km depth and is made of ~200 main sub-parallel, exceptionally exposed

129   faults (Di Toro and Pennacchioni, 2005; Mittempergher et al., 2021; Smith et al.,

130   2013). Pseudotachylytes were collected from extensional, neutral and compressional

131   structural domains along wavy fault veins and from injection veins (opening mode

132   cracks) (Fig. 3a). The injection veins are asymmetrically distributed and mostly

133   intruded the south-facing wall rock (Di Toro et al., 2005).

134   *Thin sections.* 22 natural and three experimental pseudotachylytes were cut

135   perpendicular to the slip zone and parallel to the slip direction (see Supplementary

136   Materials SM2 for the digital scans of the thin sections). The derived ~30 μm thick

137   thin sections were Syton®-polished for high resolution FESEM and EMPA analysis.

138   *Microstructural analysis* was performed with an optical petrographic microscope and

139   with a high-resolution Tescan Solaris Field Emission Scanning Electron Microscope

140   (FESEM) at the Dept. of Geosciences in University of Padova. Back Scatter

141   Electrons (BSE) and Cathodoluminescence (CL) imaging were performed at the

142   FESEM with operating conditions of: 14 mm working distance; 10 keV acceleration

143   voltage; and 3 nA beam current.

144   _Elemental analysis_ (composition of the pseudotachylyte matrix) was performed with

145   electron wavelength-dispersive microprobe analysis (EMPA) on Syton®-polished thin

146   sections at the Dept. of Geosciences in University of Padova. Data were collected

147   using 15 kV as accelerating voltage and 15 nA as beam current. The analyzed

148   volume of the thin section was 2-3 μm in diameter. Sodium and potassium were

149   analyzed first to prevent alkali migration effects. The precision of the microprobe was

150   measured through the analysis of well-characterized synthetic oxide and mineral

151   secondary standards and was better than 5% for all cations.

152   _Grain-scale fault roughness analysis_. High resolution images (10 μm pixel) of the

153   entire thin section were obtained by optical (natural pseudotachylytes) and FESEM-

154   BSE (experimental pseudotachylytes) imaging. The PST-HR boundaries of both

155   natural and experimental pseudotachylytes were manually drawn with Inkscape®

156   over a length ranging from 6.7 to 34.5 mm and with resolution of 10 μm (see

157   Supplementary Materials SM2). The resolution of the measurements (10 μm, well

158   below the average mineral grain size, ~2 mm) and the length of the digitized PST-

159   HR boundaries (greater than mineral grain size) allowed us to test whether the

160   mineral grain size, together with $\dot{Q}(t)$, controls the grain-scale roughness of the PST-

161   HR boundaries. The grain-scale roughness of the PST-HR boundaries was then

162   analyzed with a MATLAB script to determine the Fast Fourier Transform (FFT)

163   spectra, ω_0 (characteristic asperity height which corresponds to the root mean

164   square, RMS, of the PST-HR boundary height) and λ_{ave} (average asperity radius),

165   defined as:

166    $\omega_0 = \sqrt{\sum_{i=1}^{N} \frac{z_i^2}{N}}$ Eq. 1

167    $\lambda_{ave} = \sum_{i=1}^{N} \frac{\lambda_i}{N}$ Eq. 2

168   where z_i is the height of every point i of the PST-HR boundary with respect to $z = 0$,

169   defined so that $\sum_{i=1}^{N} z_i = 0$ (with N the number of points along the boundary); λ_i are

170   the radii of the circles that approximate the curvature of the surface boundary around

171   the maxima of the topography (e.g., embayments) calculated from finite differences

172   at points i-1, i, i+1 (Nielsen et al., 2010) (Fig. 1). The roughness of the PST-HR

173   boundary is described by a series of continuous trigonometric functions where, for

174   each function, the maximum amplitude z_i is $\sqrt{2}\,\omega_0$ (Panzarasa & Tribulato, 1989)

175   and the length $\sqrt{2}\omega_0$ corresponds to the maximum depth of the embayments (Fig.

176   1). The MATLAB script, the thin section scans and the drawn PST-HR boundaries

177   are available at https://researchdata.cab.unipd.it/id/eprint/725 and in Supplementary

178   Materials SM2.

3. Results

180   *3.1 Experimental pseudotachylytes*

181   In S422, S423 and S475 experiments, τ decreased from a peak value at initiation of

182   slip towards an approximately constant residual value (called "steady-state" shear

183   stress, τ_{ss}) of 2.70 MPa (at 20 MPa normal stress), 3.92 MPa (at 30 MPa) and 3.44

184   MPa (40 MPa) (Fig. 2a). These τ_{ss} correspond to $\dot{Q}_{ss}$ ($\tau_{ss}\,V_{eq\_ss}$ with V_{eq_ss} = 6.5 m s^{-}

185   ^{1}; Fig. 2b) of 17.55, 25.50 and 22.36 MW m^{-2}, respectively (Table 1). HRV376

8

186   experiment, performed at 1.3 m s^{-1}, had τ_{ss} = 3.86 MPa (Di Toro et al., 2006) that

187   correspond to $\dot{Q}_{ss}$ = 5.02 MW m^{-2}. In all the experiments, the PST-HR boundary is

188   similar on both sides of the slip zone, with embayments at HR biotite grains (Fig. 2c).

189   The experimental pseudotachylyte consists of abundant angularly shaped quartz

190   clasts and few rounded plagioclase clasts immersed in a uniform gray in color or, in

191   correspondence of biotite grains in the host rock, bright in color glassy-like matrix

192   (BSE-SEM images, Fig. 2d-e). Biotite clasts were not found in the pseudotachylyte

193   matrix. The most common gray in color matrix ("Ca-rich") is enriched in Ti, Fe, Mn,

194   Mg, and K and depleted in Si, Al, Ca and Na compared to the composition of

195   plagioclase (the reverse is true of the composition of biotite) (Table 2). The less

196   common bright in color matrix ("Fe-rich") is found next to the biotite grains in the wall

197   rocks and has a composition very similar to that of biotite (Table 2).

198

199   *3.2 Natural pseudotachylytes*

200   In many individual faults of the Gole Larghe Fault Zone, the pseudotachylytes

201   overprint cataclasites with sub-greenschists facies assemblage made of quartz,

202   plagioclase and K-feldspar clasts within a chlorite-epidote-rich matrix (Di Toro and

203   Pennacchioni, 2005; Supplementary Materials SM3). Only pseudotachylyte-bearing

204   fault segments across non-altered tonalite free of a precursor cataclasite (Di Toro et

205   al., 2006; Pittarello et al., 2008; Griffith et al., 2010) are considered here (Fig. 3). In

206   pseudotachylyte fault veins, the PST-HR boundary shows embayments at biotite

207   grains (Fig. 3b-d) and at preexisting microcracks and (pressure) dissolution seams in

208   the wall rock (Supplementary Materials SM3). Some embayments are filled by a

209   quartz-rich portion of the pseudotachylyte formed by abundant quartz clasts welded

210   by devitrified glassy matrix and microlites of biotite and plagioclase (Fig. 3b-c and

211   inset). This ultrafine aggregate is interpreted as a clast-laden melt filling the

212   embayment. However, most embayments in biotite are filled by the pseudotachylyte

213   matrix rich in biotite acicular microlites (Fig. 3d). With respect to the north-facing

214   PST-HR boundary, the southern one commonly shows (1) higher roughness (Fig.

215   3e), (2) more numerous injection veins (Di Toro et al., 2005) and, (3) more extensive

216   and scattered shattering of quartz and plagioclase grains (in contrast with discrete

217   microcracks sub-parallel to the main fault in the northern block: Fig. 3f). In injection

218   veins (Mode I cracks), the PST-HR boundaries are rougher than in fault veins (Fig.

219   3g).

220

221   *3.3 Grain-scale roughness of the pseudotachylyte-host rock (PST-HR) boundary*

222   <u>*In experimental pseudotachylytes*</u>, the magnitude and the slope of the FFT spectra

223   are unrelated to $\dot{Q}_{ss}$ (Figs. 4a and c). Moreover, λ_{ave} has a weak inverse relation with

224   ω_0 (Fig. 5a) and is unrelated to $\dot{Q}_{ss}$ (Fig. 5c) and, ω_0 decreases with increasing $\dot{Q}_{ss}$

225   (Fig. 5e, Table 3). This negative trend of ω_0 with $\dot{Q}_{ss}$ is due to the high ω_0 values of

226   the grain-scale roughness of the PST-HR boundary from experiment HVR376, which

227   was performed with a much lower $\dot{Q}_{ss}$ (5.02 MW m^{-2}) than the other experiments

228   (17.55÷25.50 MW m^{-2}) (Table 1). The ω_0 values plot along the FFT spectra of their

229   respective PST-HR boundaries (Fig. 4a), as expected by geometrical

230   argumentations (this is the case also for the spectra of the natural pseudotachylytes)

231   (Beeler, 2023).

232   <u>*In natural pseudotachylytes*</u>, the magnitude of the FFT spectra is higher in injection

233   veins and extensional domains, and lower in neutral and compressional domains

234 (Fig. 4b), the slopes of the FFT spectra are unrelated to the structural domain (Fig.

235 4d). The λ_{ave} has a weak inverse relation with ω_0 (Fig. 5b) and is unrelated to the

236 structural domain (Figs. 5d) (Table 3). The value of ω_0 is higher in the injection veins

237 than in the other structural domains with the lowest value measured in a

238 compressional domain (L05-06N) (Fig. 5f).

4. Discussion

240 We first discuss the geometry of the PST-HR boundary in both experimental and

241 natural pseudotachylytes. Then, by using the grain-scale roughness as correlating

242 factor, we estimate $\dot{Q}$ from the samples collected in fault L05 that cuts non-altered

243 tonalite. In fact, PST-HR boundaries from natural faults with preexisting microcracks

244 and dissolution seams in their wall rocks were excluded from the analysis (see

245 Supplementary Materials SM3).

246 Experimental pseudotachylytes were produced by sliding pre-cut cylinders.

247 Therefore, the large stress perturbations expected during propagation of the seismic

248 rupture tip in natural faults (e.g., Reches and Dewers, 2005) can be assumed

249 negligible. We assume that the grain-scale roughness of experimental

250 pseudotachylytes is mainly related to preferential melting of biotite. Once "steady-

251 state" slip conditions are achieved in the experiment (Fig. 2a), the isotherms are

252 approximately fixed in space (Nielsen et al., 2008). As a consequence, the solid rock

253 specimen (1) passes through the isotherms during sample rotation, (2) heats up, (3)

254 melts, (4) the melt is expelled because of the applied normal stress and centrifugal

255 forces, and (5) the sample shortens at a constant rate (Nielsen et al., 2008) (Fig. 1).

256 Under "steady-state" conditions the temperature T_z in the host rocks can be

257 calculated by combining Eq. 4 and Eq. 70 in Nielsen et al. (2008):

258 $$T_z = (T_{melt} - T_i) \exp\left(-\frac{z\tau\dot{u}}{\kappa\rho(L+c(T_m-T_i))}\right) + T_i \qquad \text{Eq. 3.}$$

259 By looking at the exponential in Eq. 3, for a given isotherm T_z, the thermal gradient in

260 the host rocks perpendicular to the fault increases with increasing $\dot{Q}$ ($= \tau\dot{u}$). The

261 formation of embayments is controlled by preferential melting of biotite (Fig. 1). In the

262 experiments the following parameters apply: melt temperature $T_{melt} = 1450°C$; rock

263 density $\rho = 2600 \text{ kg/m}^3$; latent heat $L = 3.32 * 10^5$ J/kg (Di Toro and Pennacchioni,

264 2006); ambient temperature $T_i = 20°C$; thermal diffusivity $\kappa = 5 * 10^{-7}$ m²/s for the

265 temperature range 650-1450 °C of host rock melting (considering the nominal melting

266 temperature of biotite as the lower end and the melt temperature as the higher end

267 of this temperature range; Whittington et al., 2009); and specific heat capacity $c =$

268 1500 J/kg/K (Waples and Waples, 2004).

269 In the experiments presented here, the temperature in the slip zone during frictional

270 sliding was not measured because of technical limitations of the most used

271 techniques (e.g., high speed infra-red camera or thermocouples, see discussion in

272 Aretusini et al., 2021). However, the estimated melt temperature of 1450°C is

273 consistent with the microstructural observations (Fig. 2d-e) and with the chemical

274 composition of the pseudotachylyte glass (Table 2). In fact, (1) though the host rock

275 tonalite is made by 49% plagioclase (An45), 29% quartz, 16% biotite and 6% K-

276 feldspar, the clasts that survived from melting are mostly made of quartz (melting

277 point 1730°C), while there are few plagioclase An45 clasts (melting point 1250°C,

278 Spray, 2010; Deer et al., 1992) and none of biotite (Fig. 2d) and (2) melting of biotite

279 and plagioclase melting largely contributes to the formation of the friction melt (see

280 rounding of plagioclase grains and incipient melting of biotite in Figs.2d-e). This

281 interpretation is supported by the elemental composition of the glassy matrix which

282   has a SiO_2 concentration slightly lower than the one of plagioclase but higher than

283   that of biotite and by the presence of FeO, K_2O, CaO, MgO, etc. which is consistent

284   with selective melting of plagioclase and biotite (and probably K-feldspar) (Table 2).

285   We infer that the frictional melt temperature was larger than the melting point of

286   plagioclase (1250°C estimated from the solidus of plagioclase melting T at ambient

287   pressure for An_{45} content, see Deer et al., 1992 and references therein) but lower

288   than that of quartz (1730°C, Navrotsky, 1995). The above temperature estimates, in

289   the range of 1450°C and constrained by microstructural observations and

290   geochemical investigations, are in the range of temperature estimates obtained from

291   numerical models (Supplementary Materials SM1). The temperature increase in the

292   slip zone due to shear heating was estimated using Finite Element Analysis to solve

293   time dependent thermal diffusion in 2 dimensions (Cornelio et al., 2019). In the

294   model, the heat source is the measured $\tau(t)$ $V_{eq}(t)$ and it is assumed that all the

295   mechanical energy is dissipated as heat, a condition that appears to be satisfied in

296   this experimental configuration (Niemeijer et al., 2011; Aretusini et al., 2021).

297   According to numerical modeling results, temperatures of at least 1450°C were

298   reached in all experiments, and for longer times in experiments performed with

299   higher $\dot{Q}_{ss}$ (Fig. SM1).

300   Lastly, we introduce $z = \sqrt{2}\,\omega_0$, with ω_0 calculated for each experimental PST-HR

301   boundary. The length $\sqrt{2}\omega_0$ is the distance of the bottom of the embayments from

302   the reference plane $z = 0$ and should correspond to the maximum penetration depth

303   of the isotherm responsible for biotite melting (Fig. 1). Therefore, from Eq. 3, the

304   effective melting temperature of biotite is $T_{m\,eff} = 870°C \pm 180°C$. This $T_{m\,eff}$ is

305   higher than the value $T_m = 650°C$ reported in the literature (Navrotsky, 1995). There

306   are several possible explanations for this discrepancy. One is that because of

307   kinetics effects, during the short time of the coseismic frictional heat pulse, biotite is

308   not melted down to its nominal melting temperature T_m, but to a higher temperature

309     $T_{m\,eff}$. A second explanation is related to the tribo-mechanical processes

310   responsible for the formation and evolution of grain-scale roughness. For instance,

311   (1) frictional melting may include more complex poly-phase quasi-equilibrium melting

312   processes at the asperity scale (Lee et al., 2017) or, (2) the higher asperities made

313   of quartz or feldspar may undergo continuous frictional wear, particularly where the

314   friction melt is freely extruded and melt layer is thus thin. These two tribo-mechanical

315   processes contribute to smoothing the grain-scale roughness by melting or wearing

316   out those minerals that have a higher individual melting point than biotite. Therefore,

317   the assumption that the grain-scale roughness of experimental pseudotachylytes is

318   related only to preferential melting of biotite at $T_m = 650°C$ should be relaxed to

319   include other micro-scale processes. In any case, the contribution of these second-

320   order tribo-mechanical processes in defining the grain-scale roughness does not

321   substantially alter the outcomes of our analysis as discussed below.

322   In natural pseudotachylyte-bearing faults, the extensional, neutral and compressional

323   structural domains should correspond to domains of low, intermediate and high

324   normal (effective) stresses σ_n, respectively. The nearby domains of fault L05 (Fig.

325   3a) should have recorded a similar slip history under comparable average coseismic

326   slip rates (Griffith et al., 2010). When the fault is lubricated by friction melts, the

327   frictional traction τ and, therefore, $\dot{Q}$ are expected to be higher in the compressional

328   structural domains ($\tau \propto \sigma_n^{0.25}$, Nielsen et al., 2008) than in neutral and extensional

329   ones. In the case of injection veins (mode I cracks) the frictional traction is negligible

330   and the PST-HR boundary should be mainly affected by fracturing and by melt-rock

331   interaction. In fact, in injection veins the melt temperature is independent of the

332   frictional power (here, $\dot{Q} = 0$) and, the melt, once injected, cools slowly to ambient

333   temperature as the melting front propagates in the wall rocks ("*Stefan problem*", Ch.

334   XI in Carslaw and Jaeger, 1959). This type of melt-rock interaction results in a lower

335   temperature gradient in the wall rocks and in a higher grain-scale roughness at the

336   PST-HR boundary. Consistent with this interpretation, the ω_0 values are

337   systematically higher in injection veins than in fault veins (Fig. 5f). In fault veins, the

338   grain-scale roughness of the PST-HR boundary is affected by:

1. Asymmetric and intense damage associated with the transient stress

    perturbation during the propagation of the seismic rupture front at some km s^{-1}

    (Poliakov et al., 2002). For eastward propagating ruptures of the Gole Larghe

    right-lateral strike slip faults, stress perturbation induced intense fracturing

    and wall-rock spallation especially in the southern block of individual faults (Di

    Toro et al., 2005) (Fig. 3f bottom). In contrast, the orientation of the

    microcracks in the northern wall rock is sub-parallel to the E-W strike of the

    fault (Fig. 3f top). This orientation is consistent with the direction of the

    maximum transient compressive stress associated with eastward rupture

    propagation along a right-lateral strike slip fault (Fig. 4 in Di Toro et al., 2005).

    According to this interpretation, the northern and southern blocks were

    located on the transient compression and tension stress fields, respectively, of

    the ancient rupture that propagated along this fault segment. The grain-scale

    roughness resulting from the stress perturbation at the rupture-tip is not

    included in the theoretical model which relates the grain-scale roughness to $\dot{Q}$

    (Nielsen et al., 2010);

355   2. Reworking of the PST-HR boundary due, for instance, to filling of

356   embayments by the clasts carried by the melt (Figs. 3b-c). The resulting grain-

357   scale roughness should be excluded from our analysis (see black in color line

358   in Fig. 3b).

359   3. Preferential melting of biotite with respect to the other host rock-forming

360   minerals due to non-equilibrium frictional melting. This would result in the

361   grain-scale roughness related to the $\dot{Q}$ in the process zone that is considered

362   in the theoretical analysis by Nielsen et al. (2010). We note here that grain-

363   scale roughness will thus reflect not only the heating rate of the slipping zone

364   and the associated thermal gradient in the wall rocks but also the relative

365   melting points of the various mineral phases and their grain sizes. We make

366   also the assumption that steady-state conditions during frictional melting were

367   achieved. This assumption might be partly relaxed by the evidence that in the

368   selected natural faults the pseudotachylyte matrix at the contact with the

369   biotite grains in the wall rock includes biotite microlites precipitated from the

370   melt (Fig. 3d). In addition, the embayments are laterally confined by well-

371   rounded plagioclase grains (Fig. 3d). The above microstructural evidence is

372   consistent with progressive migration of the isotherms and associated melting

373   front in the wall rock tonalite (Fig. 1), followed by crystallization of biotite

374   microlites during cooling and solidification of the melt (Fig. 3d).

375 Based on the above analysis of the physical processes that shape the PST-HR

376 boundary, we decided to use ω_0 to estimate $\dot{Q}$ within the several parameters

377 (magnitude and slope of FTT, ω_0 and λ_{ave}) that describe the grain-scale roughness

378 (Table 3). In fact, the FFT magnitude of the PST-HR boundary is affected by $\dot{Q}$ only

379 in the natural pseudotachylytes (Figs. 4a-b). Instead, the slope of the FFT is a

16

380   measure of roughness scaling across the scale of measurements (10 µm – 10's of

381   mm) and thus is not necessarily affected by $\dot{Q}$ (Beeler, 2023). Moreover, there is not

382   a clear dependence of λ_{ave} with $\dot{Q}$ or the structural domain (Figs. 5c-d). In fact, while

383   the value of ω_0 represents the roughness at the profile scale (6.7÷34.5 mm)

384   spanning ~3-17 grains and may thus be particularly sensitive to grain-scale

385   roughness, λ_{ave} is a local measure comparing neighboring profile points (across 30

386   µm), which is much smaller than the grain scale. The poor dependence of λ_{ave} with

387    $\dot{Q}$ is due to the fact that melting along sliding surfaces is the primary driver of the

388   grain-scale roughness, and, consequently, λ_{ave} depends on both grain size and

389   melting point of the individual minerals. Since the tonalites discussed here that host

390   the natural and experimental pseudotachylyte have the same average grain size,

391   λ_{ave} is poorly dependent of $\dot{Q}$. In contrast, ω_0, although like λ_{ave} varies with grain size

392   and melting point of the host rock minerals (e.g., the maximum value of ω_0 will be

393   limited by the size of the mineral with the lowest melting point), it depends also on

394   the heating rate of the slipping zone and the associated thermal gradient in the wall

395   rocks, which are proportional to $\dot{Q}$ (Fig. 1).

396   Because of the effect of the processes listed at points 1 and 2 above, to estimate $\dot{Q}$

397   we consider the northern PST-HR boundary of the samples from fault L05. In these

398   pseudotachylytes, (1) there is no evidence for sub-greenschists facies cataclastic

399   precursors (Fig. 3), and (2) the northern block was less affected by the coseismic

400   stress perturbation because located in the compression field of the eastward

401   propagating rupture (Fig. 3f, see Di Toro et al., 2005). We can reasonably assume

402   that in these samples the grain-scale roughness is mainly related to the preferential

403   melting of biotite (Fig. 3d). From the analysis of the experimental pseudotachylytes

404   the calculated melting temperature for biotite is assumed to be $T_{meff} = 870\,°C$ (Fig.

405   5e); substituting it as T_z in Eq. 3 and rearranging the equation we obtain:

406     $\tau \dot{u} = \frac{\kappa \rho \left(L + c(T_m - T_i) \right)}{\sqrt{2}\,\omega_0} \ln \left(\frac{T_m - T_i}{870°C - T_i} \right)$ Eq. 4

407   where $T_i = 250°C$ is ambient temperature during seismic faulting (Di Toro and

408   Pennacchioni, 2006). The estimated $\dot{Q}$ ($\tau\,\dot{u}$) for the natural pseudotachylytes of the

409   northern boundary of fault L05 are reported in Fig. 6. On this diagram, we also plot

410   the ω_0 vs. $\dot{Q}$ measurements for the experimental pseudotachylytes. According to this

411   analysis, natural pseudotachylytes are the result of $\dot{Q}$ ranging from 4 to 60 MW m^{-2},

412   with an arithmetic mean value of 16 MW m^{-2}.

413   These first $\dot{Q}$ estimates obtained from field and microstructural observations are in

414   the lower range of the broad $\dot{Q}$ range from 3 to 300 MW m^{-2} proposed in the literature

415   (Fig. 2 in Sibson, 1980). But these latter estimates were based on a range of

416   possible coseismic shear stress ($30 < \tau < 300$ MPa) and on-fault slip rate ($0.1 < \dot{u} <$

417   1.0 m/s) achieved at crustal seismogenic depths of about 10 km (i.e., these

418   hypocentral depths are about the same as in our study). The proposed $\dot{Q}$ estimates

419   of > 100 MW m^{-2} would have been excessive because they would have induced very

420   high temperatures in the slip zone ($> 10.000°C$), unless a relevant reduction in τ

421   during coseismic slip was considered (see Fig 4 in Sibson, 1980). Though our field

422   estimates of $\dot{Q}$ (mean value 16 MW m^{-2}) were determined in a fault patch and may

423   not be representative of the entire fault, they are supported by experimental

424   evidence and are in agreement with the hypothesis by Sibson (1980) of large

425   reduction in τ during seismic slip (Fig. 2a). In addition, the estimates of $\dot{Q}$ proposed

426   here are based on microstructural observations associated with the effects of

18

427   temperature increase in the slip zone (Figs. 1-3) rather than on approximate

428   estimates of deformation conditions during coseismic slip.

5. Conclusions

430   What is the magnitude of the frictional power $(\dot{Q})$ dissipated on a fault during an

431   earthquake? We address this question by exploiting a theoretical model which

432   relates the grain-scale roughness of the pseudotachylyte-host rock boundary

433   described by the characteristic asperity height ω_0 to $\dot{Q}$ (Nielsen et al., 2010) (Fig. 1).

434   In experimental pseudotachylytes produced under known $\dot{Q}$ (Fig. 2), ω_0 decreases

435   with increasing $\dot{Q}$ (Fig. 5e), as predicted by the model (Fig. 1). In natural

436   pseudotachylytes from the Gole Larghe Fault Zone within the Adamello tonalites, ω_0

437   is higher for injection veins (where $\dot{Q}$ should be negligible) than for extensional,

438   neutral and compressional fault domains (Fig. 5f). These domains should correspond

439   to low, intermediate and high $\dot{Q}$, respectively (Figs. 5e-f). Contrary to experimental

440   pseudotachylytes, produced by shearing precut samples, the grain-scale roughness

441   of natural pseudotachylyte PST-HR boundary is also affected by the intense damage

442   associated with the propagation of the seismic rupture tip. In the Gole Larghe Fault

443   Zone, this host rock damage is especially developed in the southern wall block.

444   Therefore, to estimate $\dot{Q}$ we considered six samples of the northern boundary of fault

445   L05. In fact, the interpretation of the microstructures (Fig. 3) suggests that the grain-

446   scale roughness of the northern side of fault L05 mainly resulted from preferential

447   melting of biotite (Fig. 3d). From the experimental dataset we estimate with Eq. 3 the

448   (effective) melting temperature $T_{m\,eff} = 870°C$ of biotite during frictional melting. This

449   estimate is based on the depth $z = \sqrt{2}\,\omega_0$ of the embayments, which should

450   correspond to the maximum penetration depth of the isotherm responsible for biotite

451   melting. Finally, by inserting $z = \sqrt{2}\,\omega_0$ in Eq. 4 for the samples from fault L05, we

452   estimate $\dot{Q}$ which ranges from 4 to 60 MW m^{-2}, with an average value of 16 MW m^{-2}.

453   These $\dot{Q}$ values are in the lower range of very broad estimates (3-300 MW m^{-2})

454   based on typical average seismic slip rates and frictional tractions inferred for the

455   upper continental crust (Sibson, 1980). In addition, these low estimates of $\dot{Q}$ would

456   suggest that the pseudotachylytes studied, at least at the scale of the fault patch

457   investigated (a few m^2), may be representative of earthquakes that have excess

458   radiated seismic energy (Beeler et al., 2016). Actually, our estimates of $\dot{Q}$ based on

459   field and microstructural observations, although valid for fault patches of few m^2 in

460   size, could be compared with $\dot{Q}$ values obtained in the rare cases where absolute

461   stress levels, and hence $\tau(t)\,\dot{u}(t)$, can be estimated (Spudich, 1992; Milliner et al.,

462   2022). However, our field-based estimates of frictional power per unit area

463   dissipated during earthquakes, although independent of assumptions about the

464   magnitude of seismic slip rates and shear tractions, may suffer from a number of

465   other assumptions as discussed above. For instance, the theoretical model does not

466   include (1) non-steady-state conditions and second order effects (e.g., latent heat of

467   melting, mineral and temperature-dependent thermal conductivity variations) which

468   may perturb the curvature of the isotherms migrating in the wall rocks (i.e., we

469   assumed planar isotherms in Fig. 1) or (2) other tribo-mechanical processes that

470   may contribute to the shaping of the grain-scale roughness. Nevertheless, the

471   approach presented here can be applied to pseudotachylytes produced in other

472   geodynamic settings and at deeper crustal levels and will help determine this

473   relevant but elusive parameter of the earthquake source.

Acknowledgements

Contributions

F. Lazari: Conceptualization, Writing - Original Draft, Methodology, Software, Formal analysis, Investigation, Data Curation. **A. Castagna:** Conceptualization, Writing - Review & Editing, Methodology, Software, Formal analysis, Investigation, Data Curation. **S. Nielsen:** Conceptualization, Writing - Review & Editing, Software, Investigation, Resources, Funding acquisition. **A.W. Griffith:** Conceptualization, Writing - Review & Editing, Methodology, Software. **G. Pennacchioni:** Writing - Review & Editing, Investigation, Resources, Funding acquisition. **R. Gomila:** Methodology, Writing – Review & Editing, Resources. **P. Resor:** Writing - Review & Editing, Methodology, Investigation, Funding acquisition. **C. Cornelio**: Review & editing, thermal modelling. **G. Di Toro:** Conceptualization, Writing - Review & Editing, Methodology, Investigation, Resources, Supervision, Project administration, Funding acquisition.

References

Andersen, T.B., Mair, K., Austrheim, A., Podladchikov Y., Vrijmoed J.C., 2008. Stress release in exhumed intermediate and deep earthquakes determined from ultramafic pseudotachylyte. Geology 36, 995–998.

Aretusini S., Núñez-Cascajero A., Spagnuolo E., Tapetado A., Vázquez C., Di Toro G., 2021. Fast and localized temperature measurements during simulated earthquakes in carbonate rocks. Geophys. Res. Lett. 48, e2020GL091856, https://doi.org/10.1029/2020GL091856

Beeler, N., Di Toro, G., Nielsen, S., 2016. Earthquake source properties from pseudotachylite. Bull. Seism. Soc. Am. 106, 2764-2776.

Beeler, N., 2023. On the scale-dependence of fault surface roughness. J. Geophys. Res. https://doi.org/10.1029/2022JB024856

Callegari, E., Brack, P., 2002. Geological map of the Tertiary Adamello batholith (Northern Italy) Explanatory notes and legend. Mem. Sci. Geol. 54, 19–49.

Carslaw, H.S., Jaeger, J.C., 1959. Conduction of Heat in Solids, 2nd edition. Oxford at the Clarendon Press, Oxford.

Cornelio C., Spagnuolo E., Di Toro G., Nielsen S., Violay M., 2019. Mechanical behaviour of fluid-lubricated faults. Nature Communications, 10.1038/s41467-019-09293-9, pp. 1-7.

Deer W.A., Howie, R.A., Zussman, J., 1992. An introduction to rock-forming minerals. 2nd Ed. Longman Scientific & Technical, Harlow (UK).

517 Di Toro, G., Pennacchioni, G., 2005. Fault plane processes and mesoscopic structure

518   of a strong-type seismogenic fault in tonalites (Adamello batholith, Southern Alps).

519   Tectonophysics 402, 55–80.

520 Di Toro, G., Nielsen, S., Pennacchioni, G., 2005. Earthquake rupture dynamics frozen

521   in exhumed ancient faults. Nature 436, 1009–1012.

522 Di Toro, G., Hirose, T., Nielsen, S., Pennacchioni, G., Shimamoto T., 2006. Natural

523   and experimental evidence of melt lubrication of faults during earthquakes.

524   Science 311, 647–649.

525 Di Toro, G., Niemeijer, A., Tripoli, A., Nielsen, S., Di Felice, F., Scarlato, P., Spada,

526   G., Alessandroni, R., Romeo, G., Di Stefano, G., Smith, S., Spagnuolo, E.,

527   Mariano, S., 2010. From field geology to earthquake simulation: a new state-of-

528   the-art tool to investigate rock friction during the seismic cycle (SHIVA).

529   Rendiconti Lincei 21, pp. 95–114.

530 Di Toro, G., Han, R., Hirose, T., De Paola, N., Nielsen, S., Mizoguchi, K., Ferri, F.,

531   Cocco, M., Shimamoto, T., 2011. Fault lubrication during earthquakes. Nature

532   471, 494–499.

533 Ferrand, T. P., Nielsen, S., Labrousse, L., Schubnel, A., 2021. Scaling seismic fault

534   thickness from the laboratory to the field. J. Geophys. Res. 126, e2020JB020694.

535 Fialko, Y., Khazan, Y., 2005. Fusion by the earthquake fault friction: stick or slip? J.

536   Geophys. Res. 110, B12407.

537 Griffith, W. A., Nielsen, S., Di Toro, G., Smith S.A.F., 2010. Rough faults, distributed

538   weakening, and off-fault deformation. J. Geophys. Res. 115, B08409.

539 Guatteri, M., Spudich P., 1998. Coseismic temporal changes of slip direction: The

540   effect of absolute stress on dynamic rupture. Bull. Seism. Soc. America 88, 777–

541   789.

542 Hirose, T., Shimamoto, T., 2005. Slip-weakening distance of faults during frictional

543   melting as inferred from experimental and natural pseudotachylytes. Bull. Seism.

544   Soc. America 95, 1666–1673.

545 Hosseinzadehsabeti, E., Ferré, E.C., Andersen, T. B., Geissman, J. W., Bilardello, D.,

546   Di Toro, G., 2021. Focal mechanisms of intraslab earthquakes: Insights from

547   pseudotachylytes in mantle units. J. Geophys. Res., e2020JB021479.

548 Johnson, S. E., Song, W. J., Vel, S. S., Song, B. R., Gerbi, C. C., 2021. Energy

549   partitioning, dynamic fragmentation, and off-fault damage in the earthquake

550   source volume. J. Geophys. Res. 126, e2021JB022616.

551 Lee, S.K., Han, R., Jeong, G.Y., Khim, H., Hirose., T., 2017. Quasi-equilibrium melting

552   of quartzite upon extreme friction. Nature Geoscience 10, 436-442.

553 Maddock, R.H., Grocott, J., Van Nes, M., 1987. Vesicles, amygdales and similar

554   structures in fault-generated pseudotachylytes. Lithos 20, 419-432.

555 Magloughlin, J.F., Spray, J.G., 1992. Frictional melting processes and products in

556   geological materials: introduction and discussion. Tectonophysics 204, 197-206.

557 Milliner, C. W. D., Aati, S., Avouac, J. 2022. Fault friction derived from fault bend

558   influence on coseismic slip during the 2019 Ridgecrest Mw 7.1 mainshock. J.

559   Geophys. Res. 127, e2022JB024519.

560 Mittempergher, S., Zanchi, A., Zanchetta, S., Fumagalli, M., Gukov, K., Bistacchi, A.,

561   2021. Fault reactivation and propagation in the northern Adamello pluton: The

562   structure and kinematics of a kilometre-scale seismogenic source. Tectonophysics

563   806, 228790.

564 Navrotsky, A., 1995. Thermodynamic properties of minerals. In: Rock Physics and

565   Phase Relations. A Handbook of Physical Constants. AGU Reference Shelf 2, pp.

566   18–32.

567 Nielsen, S., Di Toro, G., Hirose, T., Shimamoto T., 2008. Frictional melt and seismic

568   slip. J. Geophys. Res. 113, B01308.

569 Nielsen, S., Di Toro, G., Griffith W.A., 2010. Friction and roughness of a melting rock

570   surface. Geophys. J. Int. 182, 299 –310.

571 Nielsen, S., Spagnuolo, E., Violay, M., 2012. The ultimate sample preparation for

572   rotary shear experiments. Rapporti tecnici INGV, /http://istituto.ingv.it/l-ingv/

573   produzione-scientifica/rapporti-tecnici-ingv/numeri-pubblicati-2012S.

574 Niemeijer, A., Di Toro, G., Nielsen, S., Di Felice F., 2011. Frictional melting of gabbro

575   under extreme experimental conditions of normal stress, acceleration, and sliding

576   velocity, J. Geophys. Res.116, B07404.

577 Panzarasa, G., Tribulato, S., 1989. Serie di funzioni. Edizioni Tecnos Milano, pp. 124.

578 Papa, S., Pennacchioni, G., Ross, J.A., Faccenda, M., 2018. The fate of garnet during

579   (deep-seated) coseismic frictional heating: the role of thermal shock. Geology 46,

580   471-474.

581 Petley-Ragan, A., Ben-Zion, Y., Austrheim H., Ildefonse, B., Renard, F., Jamtveit, B.,

582   2019. Dynamic earthquake rupture in the lower crust. Science Advances 5,

583   eaaw0913, 1-7.

584 Pittarello L., Di Toro, G., Bizzarri, A., Pennacchioni, G., Hadizadeh, J., Cocco, M.,

585   2008. Energy partitioning during seismic slip in pseudotachylyte-bearing faults

586   (Gole Larghe Fault, Adamello, Italy). Earth Planet. Sci. Lett. 269, 131-139.

587 Poliakov, A.N..B., Dmowska, R., Rice, J.R., 2002. Dynamic shear rupture interactions

588   with fault bends and off-axis secondary faulting. J. Geophys. Res. 107 (B11),

589   2295.

590 Pozzi, G., De Paola, N., Nielsen, S.B., Holdsworth, R. E., Tesei, T., Thieme, M.,

591   Demouchy, S., 2021.Coseismic fault lubrication by viscous deformation. Nature

592   Geosciences 14**,** 437–442.

593 Reches, Z., Dewers T.A., 2005. Gouge formation by dynamic pulverization during

594   earthquake rupture. Earth Planet. Sci. Lett. 235, 361– 374.

595 Rice, J. R., 2006. Heating and weakening of faults during earthquake slip. J. Geophys.

596   Res. 111, B05311.

597 Shand, S.J., 1916. The pseudotachylyte of Parijs (Orange Free State) and its relation

598   to "trap-shotten gneiss" and "flinty crush rock". Q. J. Geol. Soc. Lon. 72, 198-221.

599 Sibson, R. H., 1975. Generation of pseudotachylyte by ancient seismic faulting.

600   Geophys. J. R. Astron. Soc. 43, 775–794.

601 Sibson, R. H., 1980. Power dissipation and stress levels on faults in the upper crust. J.

602   Geophys. Res. 85, 6239–6247.

603 Sibson, R.H., 2003. Thickness of the seismic slip zone. Bull. Seism. Soc. Am. 93, pp.

604   1169-1178.

605 Smith, S. A. F., Bistacchi, A., Mitchell, T.M., Mittempergher, S., Di Toro G., 2013. The

606   structure of an exhumed intraplate seismogenic fault in crystalline basement.

607   Tectonophysics 599, 29–44.

608 Spray, J.G., 1995. Pseudotachylyte controversy: Fact or friction? Geology 23, 1119-

609   1122.

610 Spray, J. G., 2010. Frictional melting processes in planetary materials: from

611   hypervelocity impact to earthquakes". Ann. Rev. Earth Plan. Sci. 38, 221–254.

612 Spudich, P., 1992. On the inference of absolute stress levels from seismic radiation,

613   Tectonophysics, 211, 99-106.

614 Swanson, M. T., 1992. Fault structure, wear mechanisms and rupture processes in

615   pseudotachylyte generation. Tectonophysics 204, 223–242.

616 Tullis T.E. 2015. Mechanisms for friction of rock at earthquake slip rates. In Treatise

617   on Geophysics, 2nd Edition, Ed. Kanamori H., vol. 4, pp.139-159, Elsevier.

618 Udias A., Madariaga R., Buforn E., 2014. Source mechanism of earthquakes: Theory

619   and practice. Cambridge University Press.

620 Waples D.W., Waples J.S., 2004. A review and evaluation of specific heat capacities

621   of rocks, minerals, and subsurface fluids. Part 1: Minerals and Nonporous Rocks.

622   Natural Resources Research, 13, 97-122.

623 Whittington A.G., Hofmeister A.M., Nabelek P.I., 2009. Temperature-dependent

624   thermal diffusivity of the Earth's crust and implications for magmatism. Nature

625   458, 319-321.

626

Figure & Tables Captions

Figure 1: *Conceptual model of the relation between frictional power dissipation*
($\dot{Q}$) and grain-scale roughness of the boundary between melt (PST, pseudotachylyte
once solidified) and host rock (HR) during seismic slip in a granitoid (Qz = quartz:
T_m~1730°C; Bt = biotite: *T_m~650°C; Pl = plagioclase An$_{45}$*: *T_m~1250°C; Navrotsky,*
1995; Spray, 2010; Deer et al., 1992). Red lines represent isotherms with decreasing
spacing with increasing $\dot{Q}$. **(a)** *High $\dot{Q}$: the thermal gradient is high; the host rock*
minerals melt almost at the same rate resulting in a relatively smooth PST-HR
boundary. **(b)** *Low $\dot{Q}$: the thermal gradient is low and biotite is more affected by*
melting than the other minerals; as result deep embayments (Emb) and a rugged
PST-HR boundary develop. The grain-scale roughness of the PST-HR boundary is
described by ω_0 (characteristic asperity height, Eq. 1) and λ_{ave} (average radius of
the asperities, Eq. 2). The distance $z = \sqrt{2}\,\omega_0$ corresponds to the depth of the
embayments (see also methods section). In this conceptual model, the thermal
diffusivity of melt and wall rocks is the same and latent heat of fusion is not
considered; the isotherms are approximated as planes for simplicity. In reality,
different thermal diffusivities and the latent heat of fusion exchanged during mineral
melting may perturb the parallelism of the isotherms. Modified from Nielsen et al.
(2010).

Figure 2: *Experimental pseudotachylytes and experimental data.* **(a)** *Evolution of*
frictional traction τ vs. slip distance during experiments. The black in color segment
defines τ_{ss} for experiment S475. **(b)** *Velocity function imposed to the samples in the*

four experiments. **(c)** *Photomosaic of BSE-FESEM images of experiment S475*

performed at 30 MPa normal stress. The ~3 mm long embayment is in

correspondence of the biotite grain. **(d)** *Pseudotachylyte of experiment HVR376 with*

abundant angular clasts of quartz and few rounded clasts of plagioclase (andesine or

An$_{45}$ in composition) immersed in a Ca-rich glassy matrix. **(e)** *Pseudotachylyte-host*

rock (PST-HR) boundary of experiment HVR376 with evidence of melting and

dehydration (elongated vesicles) of biotite grains. A Fe-rich glassy matrix departs

from the biotite (c to e, BSE-FESEM images. PST, pseudotachylyte; Bt, Biotite; HR,

host rock; Pl, plagioclase; Qz, quartz).

Figure 3: *Natural pseudotachylytes.* **(a)** *Drawing of the right lateral fault L05 (GPS*

point N46 10' 348'' E10 34' 864'') with sample location (blue dots). The

compressional, neutral and extensional structural domains are evidenced by dark,

intermediate and light gray-colored areas, respectively. **(b)** *Southern*

pseudotachylyte-host rock (PST-HR) boundary from an extensional domain with two

embayments on biotite grains (Bt. The embayments are partially filled by a whitish

quartz-rich pseudotachylyte (sample L05-02). **(c)** *Detail of the quartz-rich portion of*

the pseudotachylyte in (b). The PST is formed by abundant quartz clasts welded by

devitrified glassy matrix and microlites of biotite and plagioclase (see also inset;

white arrow = Pl microlites). This ultrafine aggregate is interpreted as a clast-laden

melt filling the embayment. **(d)** *Typical embayment in biotite at the PST-HR*

boundary (see profile in Fig. 3b for location). The PST matrix at the contact with the

biotite grain includes microlites of biotite crystallized from the melt, indicative of

progressive melting of the biotite grain followed by crystallization of biotite microlites

during cooling and solidification of the melt. **(e)** *Detail of the two PST-HR boundaries*

675 *from a compressional domain. The northern boundary is smoother (ω_0 = 31 μm) than*

676 *the southern one (ω_0 = 89 μm) (sample L05-06). **(f)** Host rocks located to the north*

677 *(top, poorly damaged) and south (bottom, highly damaged) boundary of a neutral*

678 *domain (sample L05-08). **(g)** PST-HR boundaries of an injection vein (sample W05-*

679 *S01). IV, injection vein; Qz, quartz; Kf, K-feldspar; Pl, Plagioclase). (3b,e,g: Micro-*

680 *images collected with polarized petrographic microscope, plane polarized light; 3c,d:*

681 *BSE-FESEM images; 3f: FESEM-CL images).*

682

683 **Figure 4***: Results of the Fast Fourier Transform (FFT) spectral analysis in*

684 *experimental and natural pseudotachylytes. **(a)** FFT spectra of the experimental*

685 *PST-HR boundaries (colored lines) with their respective ω_0 (= RMS, colored dots) vs.*

686 *PST-HR boundary length. The ω_0 values plot along the FFT spectra of their*

687 *respective PST-HR boundaries (Beeler, 2023). There are no substantial differences*

688 *between the spectra of the four experimental pseudotachylytes. **(b)** Natural faults:*

689 *FFT spectra of natural PST-HR boundaries (colored lines) with their respective ω_0 (=*

690 *RMS, colored dots). For displaying purposes, only one spectrum from each structural*

691 *domain is reported (See Supplementary Material SM2 for the entire dataset). The*

692 *ω_0 values plot along the FFT spectra of their respective PST-HR boundaries. The*

693 *FFT magnitude is higher in injection veins and extensional domain and lower in*

694 *neutral and compressional domains. **(c)** Slope of the FFT spectra regression line of*

695 *experimental PST-HR boundaries. There is no significant variation of the slope with*

696 *increasing dissipated power. **(d)** Slope of the FFT spectra regression line of natural*

697 *PST-HR boundaries of this study. As for the experiments, there is no clear*

698 *correlation between the slopes and the structural domains. The stress normal to the*

699   *fault increases from extensional to compressive structural domains. Hence, in*

700   *natural faults, $\dot{Q}_{ss}$ should also increase toward the right on the x-axis (see*

701   *discussion).*

702

703   **Figure 5***: Grain-scale roughness of the PST-HR boundary in experimental and*

704   *natural pseudotachylytes (see Fig. 1 and Eqs. 1 and 2 for definition of ω_0 and λ_{ave}).*

705   *Sample locations and structural domains of the natural pseudotachylytes from the*

706   *northern PST-HR fault L05 (black circles, see also discussion about these*

707   *highlighted data) are reported in Fig. 3a.* **(a)** *λ_{ave} vs. ω_0 in experimental*

708   *pseudotachylytes.* **(b)** *λ_{ave} versus ω_0 in natural pseudotachylytes.* **(c)** *λ_{ave} as*

709   *function of $\dot{Q}_{ss}$ in experimental pseudotachylytes.* **(d)** *λ_{ave} plotted for different*

710   *structural domains in natural pseudotachylytes from this study.* **(e)** *ω_0 as function of*

711   *$\dot{Q}_{ss}$ in experimental pseudotachylytes. The solid black line is the distance $z_{T=870°C}/$*

712   *$\sqrt{2}$. T=870°C corresponds to the calculated melting temperature $T_{m\,eff}$ for biotite,*

713   *derived from the depth of the embayments (see discussion); gray in color dashed*

714   *lines denote the standard deviation. The values of experimental $\dot{Q}_{ss}$ are reported in*

715   *Table 1.* **(f)** *ω_0 estimates for injection veins and for the different structural domains of*

716   *fault veins in natural pseudotachylytes from this study.*

717

718   **Figure 6***: Frictional power dissipation ($\dot{Q}$) range estimated for the fault segment L05*

719   *using the grain-scale roughness of the northern pseudotachylyte-host rock boundary*

720   *(gray dots) together with the calculated frictional power dissipation derived from the*

721   *experimental pseudotachylytes of this study (black dots) and of Di Toro et al. (2006)*

722   *(diamonds). The estimate is based on the melting temperature of biotite derived from*

723   *the experimental pseudotachylytes (*$870\,°C \pm 180\,°C$*, Fig. 5d).*

724

725   ***Table 1****: Experimental data: target velocity, imposed normal stress, measured peak*

726   *and steady-state shear stress and calculated power per unit area. (*) experiment*

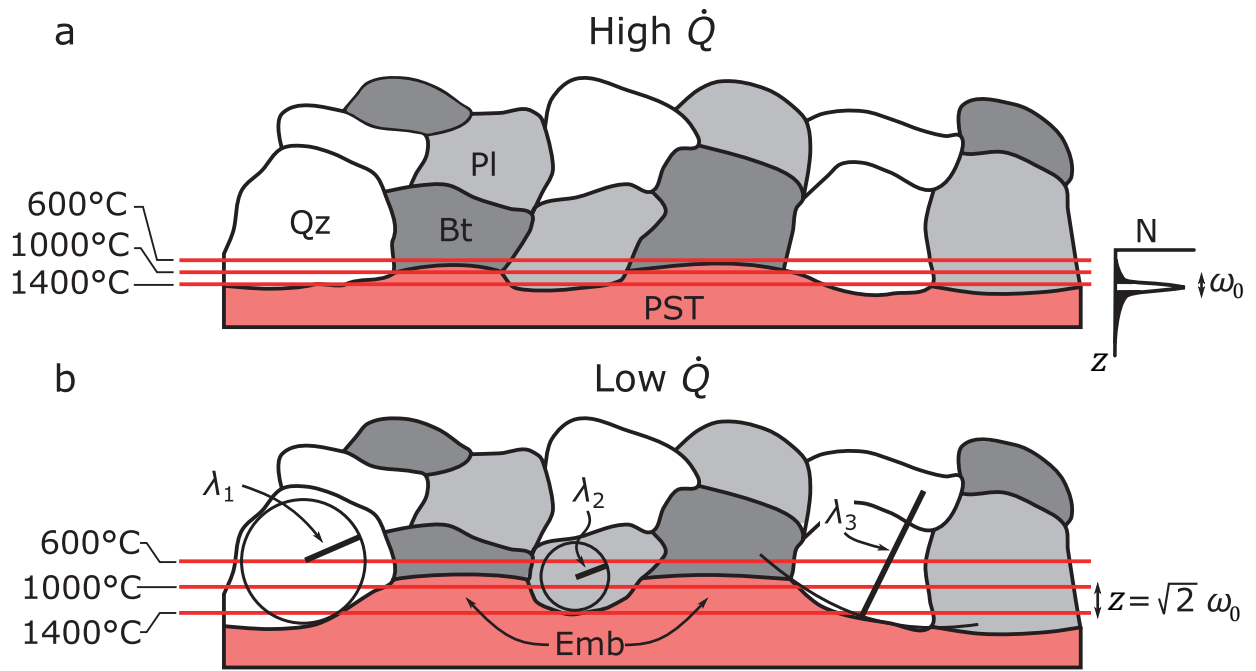727   *published in Di Toro et al., 2006.*

728

729   ***Table 2:*** *Electron microprobe analysis (EMPA) of experimental pseudotachylytes:*

730   *(s.d. = standard deviation). Plagioclase and biotite compositions are from Di Toro*

731   *and Pennacchioni, 2004) and were obtained with the same electron microprobe and*
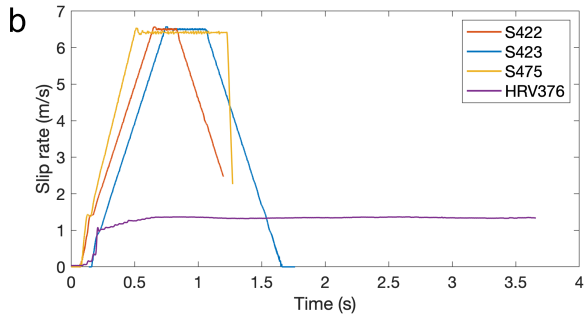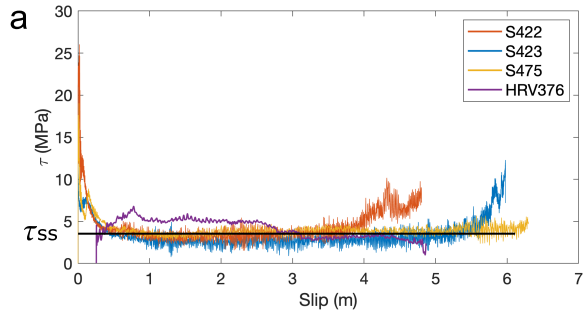
732   *working conditions.*

733

734   ***Table 3****: Grain-scale roughness parameters of the experimental and natural samples*

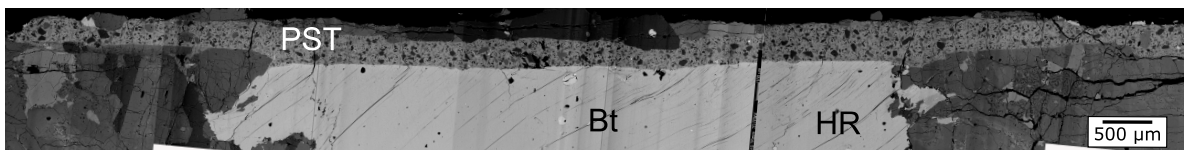735   *analyzed in this study.*

736

a   High $\dot{Q}$

600°C
1000°C
1400°C

Qz   Pl   Bt

PST

N

ω_0

z

b   Low $\dot{Q}$

λ_1 λ_2 λ_3

600°C
1000°C
1400°C

Emb

$z = \sqrt{2}\,\omega_0$

Lazari et al. Figure 1

a

b

c Experiment S475

PST

Bt   HR

500 μm

Experiment HVR376

d

Pl   Qz

Ca-rich PST
matrix

25 μm

e

Qz

Fe-rich PST
matrix

HR

25 μm
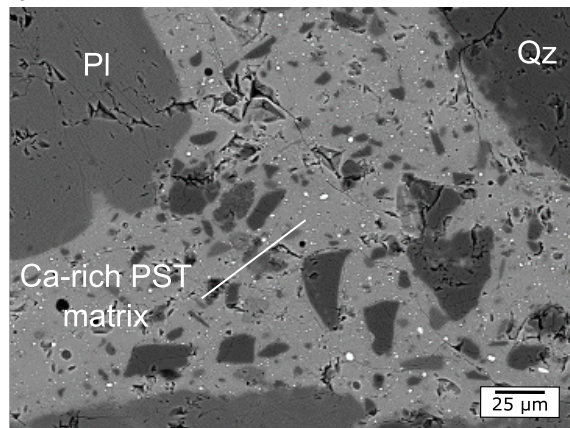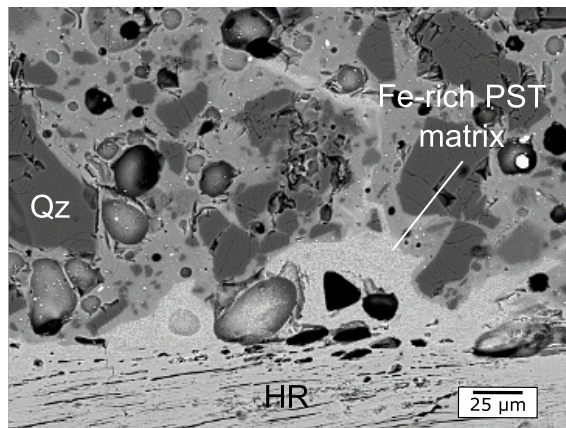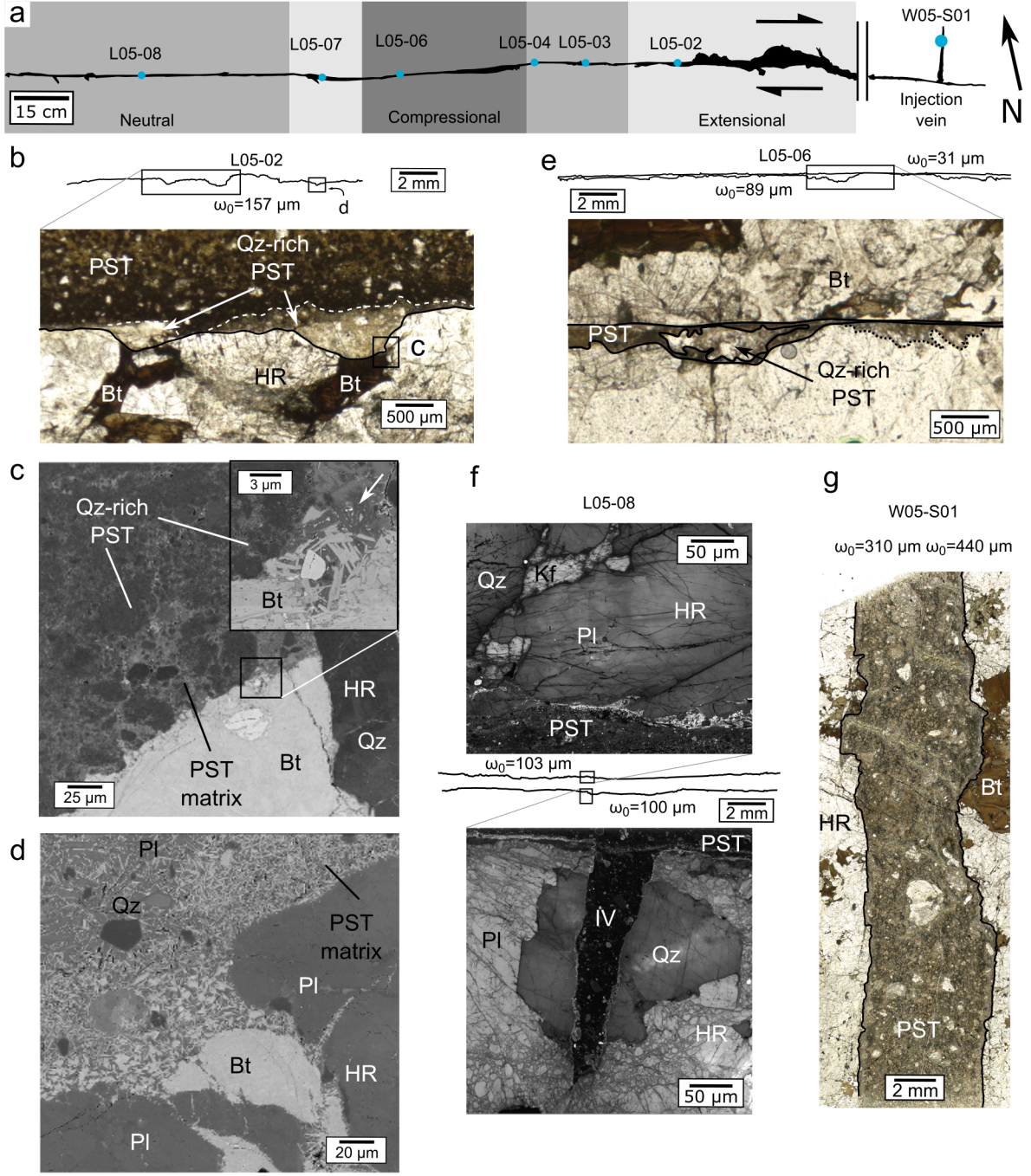
Lazari et al. Fig. 2
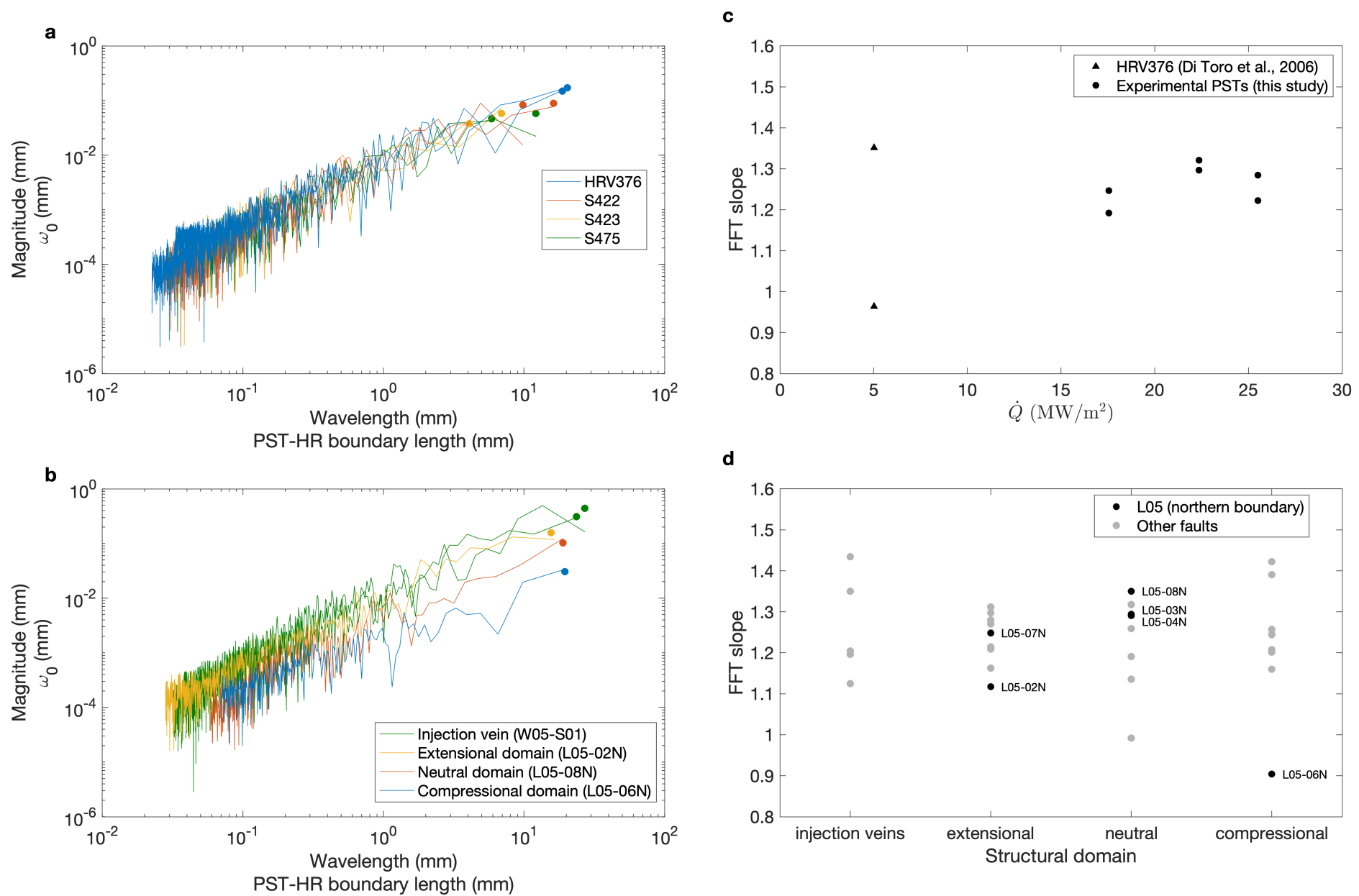
Lazari et al. Fig.3

Lazari et al. Fig. 4
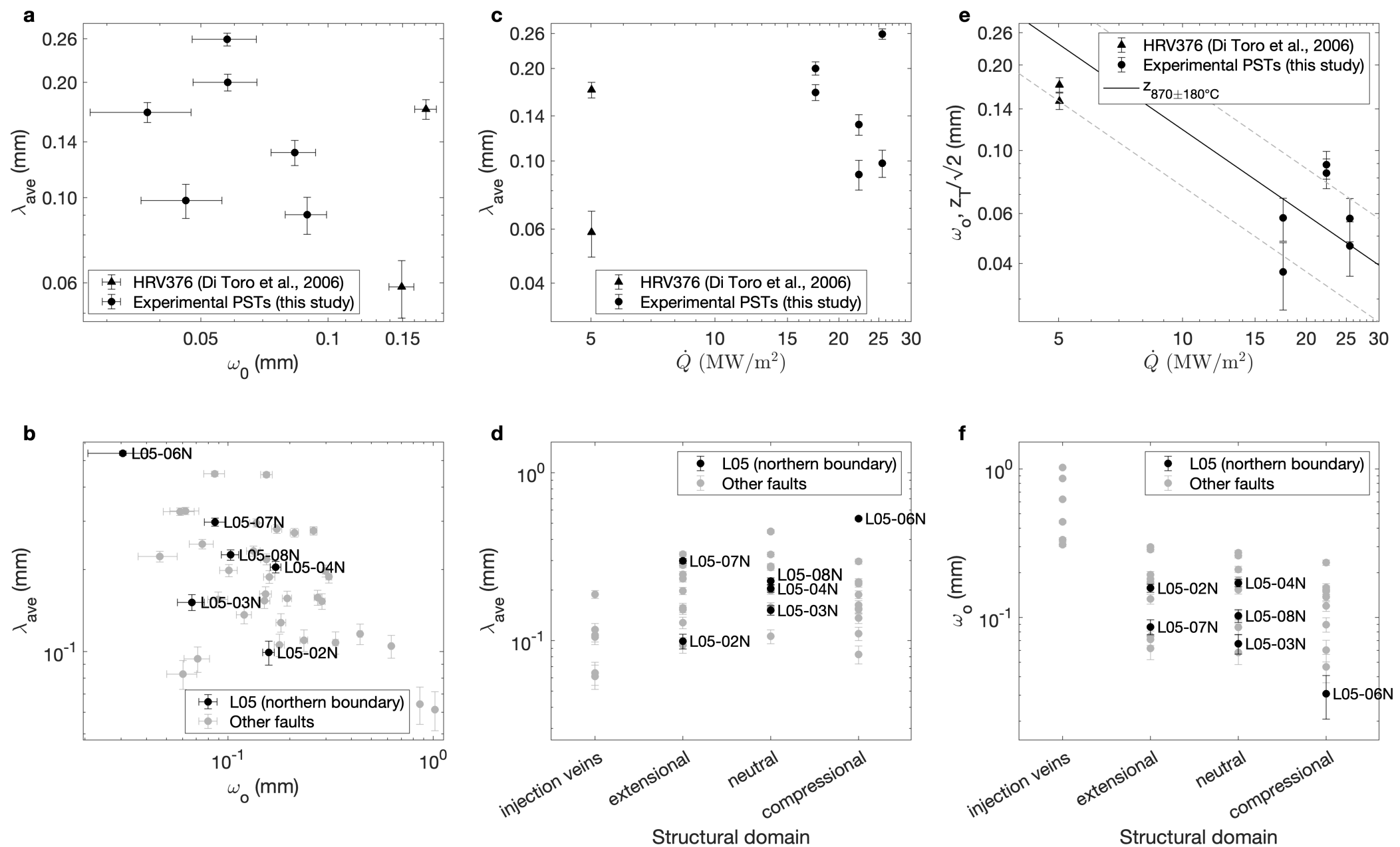
Lazari et al. Fig. 5
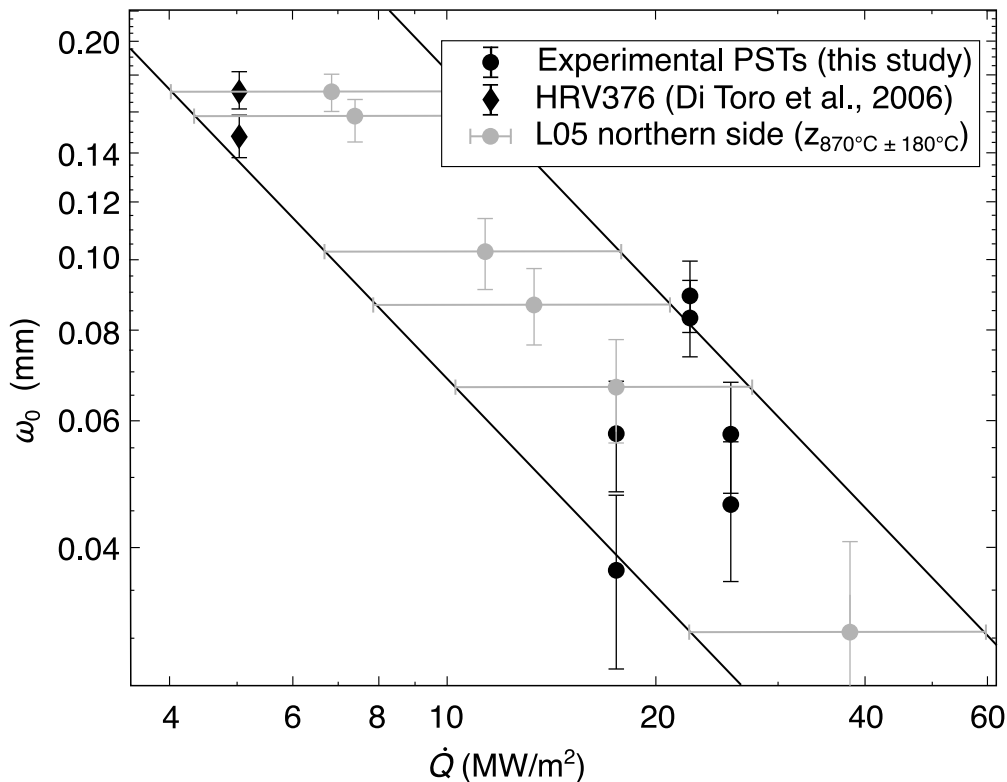
Lazari et al. Fig. 6

Table 1: *Experimental data: target velocity, imposed normal stress, measured peak and steady-state shear stress and calculated power dissipation per unit area. (*) experiment published in Di Toro et al., 2006.*

Experiment	Target velocity V_{eq_ss} (m s^{-1})	Normal stress σ_n (MPa)	Peak shear stress τ_p (MPa)	Steady-state shear stress τ_{ss} (MPa)	Power per unit area $\dot{Q}_{ss} = \tau_{ss}\, V_{eq\_ss}$ (MW m^{-2})
HRV376*	1.3	20	6.784	3.86	5.02
S422	6.5	40	26.04	3.44	22.36
S423	6.5	20	12.29	2.70	17.55
S475	6.5	30	19.05	3.92	25.50

Table 2: *Electron microprobe analysis (EMPA) of experimental pseudotachylytes: (s.d. = standard deviation). Plagioclase and biotite compositions are from Di Toro and Pennacchioni, 2004) and were obtained with the same electron microprobe and working conditions.*

	PST matrix (Ca-rich)		PST matrix (Fe-rich)		Plagioclase*		Biotite*	
	6 data	s.d.	2 data		15 data	s.d.	12 data	s.d.
SiO_2	52.21	0.39	37.58		56.20	1.28	35.45	0.19
TiO_2	1.16	0.07	2.73		0.02	0.01	2.55	0.50
Al_2O_3	22.11	0.30	17.82		26.96	0.94	17.33	0.20
FeO_{tot}	7.71	0.27	21.53		0.38	0.29	20.59	0.42
MnO	0.26	0.04	0.59		0.12	0.11	0.01	0.01
MgO	3.92	0.20	9.73		0.02	0.01	9.04	0.46
CaO	4.84	0.19	0.08		9.33	1.02	0.03	0.04
Na_2O	2.88	0.18	0.62		5.98	0.62	0.08	0.02
K_2O	4.18	0.14	8.27		0.53	0.22	9.33	0.44
Tot	99.26	0.11	98.94		99.54	0.76	94.43	0.88

*Data from Di Toro and Pennacchioni (2004)

Table 3: *Grain-scale roughness parameters of the experimental and natural samples analyzed in this study.*

Sample	λ_{ave} (mm)	λ_{ave} deviation (mm)	ω_0 (mm)	ω_0 deviation (mm)	FFT slope (adimen.)	FFT intercept (mm)	$\dot{Q}_{ss}$ (MW m^{-2}) or structural domain
HRV376 top	0.1702	0.1714	0.1703	0.1768	0.9639	-5.2620	5.020
HRV376 bot	0.0586	0.0511	0.1493	0.1463	1.3516	-4.5176	5.020
S422 top	0.1312	0.1540	0.0833	0.0772	1.3211	-4.6116	22.36
S422 bot	0.0903	0.0796	0.0892	0.0865	1.2966	-5.1414	22.36
S423 top	0.1671	0.1398	0.0374	0.0341	1.2463	-4.7004	17.55
S423 bot	0.2000	0.2039	0.0579	0.0578	1.1918	-5.2449	17.55
S475 top	0.0983	0.0538	0.0461	0.0481	1.2846	-4.7907	25.50
S475 bot	0.2590	0.2705	0.0577	0.0606	1.2220	-5.1841	25.50
A1E	0.1047	0.1319	0.6252	0.6059	1.4345	-3.7856	injection vein
A1W	0.1080	0.1357	0.3346	0.3595	1.2042	-4.3912	injection vein
A02-02N	0.2474	0.2072	0.0747	0.0797	1.2144	-5.4969	neutral
A02-02S	0.0941	0.0999	0.0710	0.0702	1.2975	-4.4707	neutral
A02-04N	0.1364	0.1522	0.1197	0.1156	1.2074	-5.2784	compressional
A2E	0.0642	0.0641	0.8621	0.8853	1.1964	-4.4267	injection vein
A2W	0.0613	0.0831	1.0217	1.0851	1.3500	-4.5118	injection vein
A4N	0.2769	0.2175	0.2613	0.2588	1.3176	-5.5750	neutral
A4S	0.1578	0.1396	0.2729	0.2554	1.1910	-4.9211	neutral
A5N	0.1277	0.1259	0.1812	0.1848	1.2490	-5.4868	extensional
A5S	0.2333	0.2149	0.1331	0.1431	1.2801	-5.2390	extensional
A7N	0.1625	0.1625	0.1525	0.1396	1.2450	-5.4098	compressional
A7S	0.2957	0.1966	0.1374	0.1376	1.2016	-5.5869	compressional
L05-02N	0.0992	0.1138	0.1577	0.1601	1.1171	-4.8767	extensional
L05-03N	0.1515	0.1470	0.0666	0.0643	1.2943	-5.0969	neutral
L05-04N	0.2039	0.2184	0.1707	0.1552	1.2910	-5.0811	neutral
L05-04S	0.1059	0.1073	0.1780	0.1750	1.2922	-4.3669	neutral
L05-06N	0.5323	0.2699	0.0307	0.0341	0.9041	-6.3854	compressional
L05-06S	0.1553	0.2183	0.0895	0.0773	1.1598	-5.1893	compressional
L05-07N	0.2979	0.2356	0.0864	0.0816	1.2482	-4.8399	extensional
L05-07S	0.3271	0.2671	0.0619	0.0584	1.1624	-4.6570	extensional
L05-08N	0.2260	0.1991	0.1027	0.0955	1.3502	-5.4975	neutral
L05-08S	0.1982	0.1682	0.1008	0.0945	1.2591	-5.6017	neutral
L09-01aN	0.1527	0.1740	0.2870	0.2872	1.2703	-4.9312	extensional
L09-01aS	0.1974	0.1759	0.2986	0.3298	1.2092	-4.9801	extensional
L09-02aN	0.1877	0.1522	0.1589	0.1578	1.2573	-5.1675	compressional
L09-02aS	0.2178	0.2046	0.1540	0.1408	1.2445	-5.3854	compressional

L09-02bN	0.2230	0.2191	0.0464	0.0429	1.1145	-5.9520	compressional
L09-02bS	0.0827	0.0883	0.0602	0.0544	1.2487	-4.8847	compressional
L09-03aN	0.2723	0.3508	0.2109	0.1974	1.1890	-5.6802	neutral
L09-03aS	0.4446	0.2220	0.1541	0.1720	0.9918	-5.5594	neutral
L09-03bN	0.3253	0.2289	0.0582	0.0554	1.1462	-5.5622	neutral
L09-03bS	0.4476	0.4125	0.0859	0.0798	1.1353	-5.0145	neutral
W05-S01E	0.1162	0.1509	0.4403	0.4540	1.3453	-4.6167	injection vein
W05-S01W	0.1882	0.1789	0.3100	0.2837	1.1248	-4.3834	injection vein
W05-S04N	0.1565	0.1735	0.1941	0.1963	1.2653	-5.5436	extensional
W05-S04S	0.2812	0.2011	0.1728	0.1752	1.3115	-4.5132	extensional
W09-S01N	0.1100	0.1293	0.2344	0.2318	1.3903	-4.8358	compressional
W09-S01S	0.1537	0.1201	0.1502	0.1541	1.4221	-5.1237	compressional